

Wide Binary Effects on Asymmetries in Asymptotic Giant Branch Circumstellar Envelopes

Hyosun Kim¹ and Ronald E. Taam^{1,2}

ABSTRACT

Observations of increasingly higher spatial resolution reveal the existence of asymmetries in the circumstellar envelopes of a small fraction of asymptotic giant branch (AGB) stars. Although there is no general consensus for their origin, a binary companion star may be responsible. Within this framework, we investigate the gravitational effects associated with a sufficiently wide binary system, where Roche lobe overflow is unimportant, on the outflowing envelopes of AGB stars using three dimensional hydrodynamic simulations. The effects due to individual binary components are separately studied, enabling investigation of the stellar and circumstellar characteristics in detail. The reflex motion of the AGB star alters the wind velocity distribution, thereby, determining the overall shape of the outflowing envelope. On the other hand, the interaction of the companion with the envelope produces a gravitational wake, which exhibits a vertically thinner shape. The two patterns overlap and form clumpy structures. To illustrate the diversity of shapes, we present the numerical results as a function of inclination angle. Not only is spiral structure produced by the binary interaction, but arc patterns are also found that represent the former structure when viewed at different inclinations. The arcs reveal a systematic shift of their centers of curvature for cases when the orbital speed of the AGB star is comparable to its wind speed. They take on the shape of a peanut for inclinations nearly edge-on. In the limit of slow orbital motion of the AGB star relative to the wind speed, the arc pattern becomes nearly spherically symmetric. We find that the aspect ratio of the overall oblate shape of the pattern is an important diagnostic probe of the binary as it can be used to constrain the orbital velocity of the AGB star, and moreover the binary mass ratio.

Subject headings: circumstellar matter — hydrodynamics — stars: AGB and post-AGB — stars: late-type — stars: mass-loss — stars: winds, outflows

¹Academia Sinica Institute of Astronomy and Astrophysics, P.O. Box 23-141, Taipei 10617, Taiwan; hkim@asiaa.sinica.edu.tw

²Department of Physics and Astronomy, Northwestern University, 2131 Tech Drive, Evanston, IL 60208; r-taam@northwestern.edu

1. INTRODUCTION

Stars coevolve with their companion in binary (or multiple) systems. On the main-sequence, about 50% of solar-type stars possess companions, and their orbital separations show a log-normal distribution from 0.01 AU to 10^4 AU with the peak at about 30 AU, or a binary period of 300 years (Raghavan et al. 2010). For evolved stars particularly in the asymptotic giant branch (AGB) phase, however, the significant extinction due to the dense circumstellar envelopes makes the direct detection of the companions difficult. After ejection of the envelope, a fraction of stars in the post-AGB and planetary nebula (PN) phases reveal evidence of binarities, although the samples are biased to the optically bright objects without strong stellar pulsations (see van Winckel 2003; De Marco 2009, and references therein). The number of known binary systems in the phase from AGB to PN is yet far from being statistically meaningful to be compared with the binary fraction and orbital period of stars on the main-sequence.

Binaries are believed to play a crucial role in the stellar evolution beyond the main-sequence (Huggins 2007; De Marco 2009). Of particular interest is the companion’s role in facilitating the shape transition from AGB to PN phases. The circumstellar envelopes of AGB stars were often observed (and assumed) to be spherical (e.g., Neri et al. 1998), while the observed PNs show a stunning variety of shapes including jets and tori (e.g., Balick & Frank 2002; De Marco 2009). In order to explain the shape transformation from AGB to PN, several scenarios including magnetic winds (e.g., Nordhaus & Blackman 2006; Pascoli & Lahoche 2010), mergers of stellar and substellar companions (Soker 1996; Nordhaus & Blackman 2006), and wind accretion around binary stars (e.g., Morris 1987; Theuns & Jorissen 1993; de Val-Borro et al. 2009; Mohamed & Podsiadlowski 2011) have been suggested. Interestingly, most of the plausible scenarios favor the existence of companions (Huggins 2007) and observationally the connection between most of the PNs and bipolar morphologies is found (Miszalski et al. 2009).

The origin and onset of the aspherical geometry remains one of the fundamental questions in stellar evolution. A small number of AGB and post-AGB circumstellar envelopes have revealed their aspherical morphologies in spectropolarimetric observations (Johnson & Jones 1991; Trammell et al. 1994) and in the nascent bipolar reflection nebulae in near-infrared polarization imagings (e.g., Schmidt et al. 2002). Some asymmetric fluctuation of the wind are traced by higher angular resolution observations of molecular line transition emission (e.g., Castro-Carrizo et al. 2010, with order of $1''$ resolution). With the subarcsecond resolutions of the Extended Very Large Array and the Atacama Large Millimeter/submillimeter Array, it is anticipated that a larger sample of AGB stars with asymmetric circumstellar envelopes will be found.

The central region of a binary system could be complex, depending on the binary separation and the size of wind acceleration zone. Close binary systems in which the AGB star fills its Roche lobe may encounter the common envelope phase (e.g., Iben & Livio 1993; Taam & Sandquist 2000). In the cases of low mass companions, spin-orbit tidal interaction will lead to its migration and spiral in (e.g., Darwin 1879; Nordhaus et al. 2010), leading to the common envelope phase. In wider binary

systems that avoid the common envelope interaction, the wind may be affected by the gravitational potential of the AGB star before reaching the Roche lobe (Mohamed & Podsiadlowski 2011) if the radiative acceleration is insufficient to ensure escape, possibly occurring in oxygen-rich outflows (Winters et al. 2000). Studying the innermost part of the wind is important for understanding the direct binary interaction, however there are many difficulties. First, most of the AGB circumstellar envelopes are extremely dense because of the substantial rates of mass loss (10^{-7} – $10^{-4} M_{\odot} \text{ yr}^{-1}$). As a result, the direct detection of the binary companion is challenging. Second, to investigate the gas accretion process, high spatial resolution for line transition observations is required. The highest resolution is about $0''.1$, corresponding to 100 AU scale at a distance of 1 kpc. At 100 AU, the escape velocity from a $1 M_{\odot}$ star is about 4 km s^{-1} , and thus a detectable binary system of this separation is unlikely to experience mass transfer via Roche lobe overflow unless the wind is slower than or comparable to 4 km s^{-1} . Since oxygen-rich winds are typically slow (Winters et al. 2000; Fong et al. 2006, e.g., Mira), it may be possible to detect the wind Roche lobe overflow (Mohamed & Podsiadlowski 2011) with current high resolution observation. It will be necessary to extend the investigation of such objects beyond 1 kpc in order to obtain a statistically meaningful sample of AGB binary systems to overcome the short AGB timescale ($\sim 10^6$ years).

On a larger scale, several theoretical and numerical works have shown that the orbital motion of binary stars deforms the geometry of the mass loss, producing a spiral pattern in the orbital plane (e.g., Soker 1994; Mastrodemos & Morris 1999; He 2007; Edgar et al. 2008; Raga et al. 2011). Particularly important was the observational discovery of a well-defined Archimedes spiral pattern in the circumstellar envelope of AFGL 3068 in dust scattered light, strongly suggesting the existence of a companion to this evolved star (Mauron & Huggins 2006). The binary scenario for this spiral pattern is strongly supported by a detection of two point sources in the near-infrared (Morris et al. 2006). Such a binary scenario has also been discussed as a possible explanation for the asymmetries emerging from the molecular line emission of CIT 6 (Dinh-V.-Trung & Lim 2009) and the dust thermal emission in the far-infrared of Mira (Mayer et al. 2011) and IRC+10216 (Decin et al. 2011).

The circumstellar spiral pattern imprinted over a large scale is of significant importance because it preserves the information of the binary hidden in the deep central part of the dense circumstellar envelope. Wide binary systems are of particular interest in testing the binary-spiral scenario as their long orbital periods induce the spiral arm spacings sufficient to be resolved by current observational techniques. For close binary stars encountering the common-envelope interactions, the overall mass loss geometry on a larger scale is likely affected by their complex evolution in the very central region. Nevertheless, the study of the spiral patterns in wide binary systems will facilitate the understanding of their binary systems.

To interpret the large spacing observed in the circumstellar patterns of AGB and post-AGB stars (e.g., 2300 AU in AFGL 3068 for an assumed distance of 1 kpc), we focus on a wide binary system, where the system is detached and Roche lobe overflow is unimportant. In a wide comparable-mass binary system, the companion star influences the mass outflow in two ways.

The companion focuses a fraction of the wind material via its gravitational potential, building a gravitational density wake (Kim 2011; Kim & Taam 2012a, KT12 hereafter) similar to the Bondi-Hoyle-Lyttleton process (Hoyle & Lyttleton 1939; Bondi & Hoyle 1944; Bondi 1952). In addition, the companion indirectly affects the geometry of the wind by forcing the AGB star to move about the center of mass of the system, thereby breaking the spherical symmetry of the outflowing wind (e.g., Soker 1994, S94 hereafter).

In order to determine the anisotropy of the wind due to the reflex motion of the mass losing star, S94 performed a coordinate transformation from the rest frame of the star to the center of mass frame of the system. S94 found the conversion factor between the solid angles in these two coordinate systems, which modifies the mass loss geometry. He (2007) extended this work and examined the dependence of the column density patterns on model parameters. A simple piston model, which provides a reasonable approximation for the structure at large distances, was employed to increase the computational efficiency. Various shapes were shown which depended on the viewing angle and the eccentricity of the binary orbit. In addition, a qualitative description for the strength of the pattern density was presented in terms of the ratio between the wind and orbital velocities. A quantitative investigation is needed to provide an interpretative framework for the observed AGB patterns, taking into account the effect of the masses of both stars and the gas pressure of the wind material (ignored in the models of S94 and He 2007).

Mastrodemos & Morris (1999) investigated smoothed particle hydrodynamic simulations of such systems taking into account the gravitational influences of the binary stars, a fictitious force to accelerate the gas in the dust formation zone, and heating and cooling mechanisms. This seminal work was especially prescient in showing the role of evolved stars in binary systems in producing a spiral shock pattern. Close binary cases in which the wind is not efficiently accelerated to the escape velocity were also investigated, which revealed significant focusing of the wind material onto the orbital plane, mimicking bipolar outflows, in addition to the spiral pattern in the orbital plane. However, their inclusion of complex physical processes in the circumstellar envelope obscured the main physical reason of the various pattern shapes.

In a subsequent study, Edgar et al. (2008) used a grid based code and reduced the complexities of the input physics, primarily focusing on the effects associated with the binary motions. By adjusting the gravitational softening radius of the companion, it was found that the overall density structure arises from the reflex motion of the mass losing star, but that the spiral shock temperature is governed by the companion. Considering that the wind speed adopted in their simulations is extremely fast (38 and 65 km s⁻¹) compared to the reflex motion of the mass losing star (of order 3 km s⁻¹), the effect of reflex motion is considerably suppressed. In contrast, the density contrast of the companion’s gravitational wake does not strongly depend on the wind velocity in the fast wind regime (see Equation (17) of KT12).

Here, we separately examine the effects of the orbital motions of the individual stars in a binary system on the structure of the outflowing envelope, enabling us to investigate the binary stellar and

circumstellar properties in detail. We first focus on the hydrodynamic effects associated with the reflex motion of the AGB star in detail, by suppressing the direct influence of companion’s gravitational potential. With an understanding of the mass flow variation due to the reflex motion, we then include the gravitational wake of the companion. In a previous paper (KT12), we investigated the gravitational wake of a low mass companion such as a planet or a brown dwarf, which does not induce the AGB star to revolve about the center of mass of the system. We will show that the results in KT12 can be applied to a system characterized by components of comparable mass.

This paper is organized as follows. In Section 2, we first revisit the analytical study of S94 in order to obtain the magnitude of the density and velocity fluctuations in the mass loss geometry without considering hydrodynamic effects. In Section 3, we describe the numerical setup for the three dimensional hydrodynamic simulations, defining the symbols and terms used in this paper. In Section 4, we present our findings from the results of the hydrodynamic simulations studying the wind velocity (Section 4.1), the density profile (Section 4.2), the morphology (Section 4.3), and the effects of companion’s gravitational wake (Section 4.4). In Section 5, we apply our model to constrain the binary orbital properties of a carbon-rich binary system, AFGL 3068. We summarize and conclude in Section 6.

2. GEOMETRICAL EFFECTS OF REFLEX MOTION OF MASS LOSING STAR: ANALYTIC ANALYSIS

We start by describing the geometrical effects of the orbital motion of a mass losing star on the density and velocity of its circumstellar envelope. Figure 1 is a schematic diagram displaying the geometrical change of a velocity element in the stellar wind. The stellar mass loss is assumed to be intrinsically isotropic with a wind velocity of \vec{V}'_w , radially expanding in the rest frame of the mass losing star. Under the influence of the gravitational potential of the secondary star, the orbital reflex motion of the mass losing star alters the direction and magnitude of the wind velocity in the center of mass frame to $\vec{V}_w = \vec{V}'_w + \vec{V}_p$, where \vec{V}_p is the orbital velocity. In order to indicate the velocity directions and to avoid confusion with the observation position (r, θ, ϕ) , we define the spherical angles relevant to the location of the mass losing star as ϑ and φ . Thus, the directions for the intrinsic wind velocity \vec{V}'_w and the wind velocity in the center of mass frame \vec{V}_w are denoted by (ϑ', φ') and (ϑ, φ) , respectively. As shown in Figure 1, as an example, the intrinsic velocity of a wind parcel \vec{V}'_w perpendicular to the orbital velocity \vec{V}_p in the orbital plane ($\vartheta' = \pi/2$; $\varphi' = \phi_p$) corresponds to the wind velocity observed in the center of mass frame having the magnitude of $V_w = (V_w'^2 + V_p^2)^{1/2}$.

As a result, the solid angle of a wind parcel is consequently modified. The wind parcel ejected from the star in the solid angle $d\Omega'$ is shifted laterally due to the inertia of the flow with the orbital velocity of the mass losing star. The projected area normal to the direction of \vec{V}_w is smaller by a factor of (V_w'/V_w) . From the definition of a solid angle, the area at a unit distance from the star is multiplied by $(V_w'/V_w)^2$. Hence, the solid angles between the intrinsic wind ($d\Omega'$) and the

wind observed in the center of mass frame ($d\Omega$) satisfy the relationship of $d\Omega = (V'_w/V_w)^3 d\Omega'$ for the wind parcel intrinsically perpendicular to the orbital motion. We note that the orbital reflex motion of the mass losing star changes not only the magnitude of the wind velocity but also the mass loss geometry (i.e., mass loss rate \dot{M}_p per solid angle). This leads to a density in the direction of \vec{V}_w for the wind parcel in Figure 1 given as

$$\rho_{\text{parcel}} = \frac{1}{r^2 V_w} \frac{d\dot{M}_p}{d\Omega} = \left(\frac{V_w}{V'_w}\right)^2 \frac{\dot{M}_p}{4\pi r^2 V'_w}, \quad (1)$$

making the relatively faster wind parcel relatively denser¹. Compared to the density distribution around the corresponding single star, $\rho' = \dot{M}_p/(4\pi r^2 V'_w)$, the contribution of this wind parcel emerging from the star with the reflex motion to the density enhancement ratio, $\rho_{\text{parcel}}/\rho' - 1$, is $(V_p/V'_w)^2$. Similarly, simple geometrical analysis leads to the result that the wind parcels in the forward and backward directions ($\varphi' = \phi_p \pm \pi/2$) have maximum and minimum values for wind matter in the center of mass frame for velocities ($V_w = V'_w \pm V_p$) and density enhancement ratios ($\pm V_p/V'_w$), respectively.

To use S94's analytic model as a basis for the analysis of our hydrodynamic simulations, we relax his linear assumption ($V_p \ll V'_w$) and fully derive the modulation of the velocity and density of material released from the AGB star in its orbital motion. However, this simple analysis is used to track a parcel in each direction, but does not take account of the interaction between the parcels emerging from the star at different positions in the orbital motion. Our numerical simulation indeed exhibits the departures from the prediction based on this simple analysis.

3. NUMERICAL METHOD

The FLASH3 code is used to solve the governing equations of hydrodynamics

$$\frac{\partial \rho}{\partial t} + \vec{\nabla} \cdot (\rho \vec{V}) = 0, \quad (2)$$

and

$$\frac{\partial \vec{V}}{\partial t} + \vec{V} \cdot \vec{\nabla} \vec{V} = -\frac{c_s^2}{\rho} \vec{\nabla} \rho - \vec{\nabla} \Phi_p^{\text{eff}} - \vec{\nabla} \Phi_{\text{comp}}. \quad (3)$$

where we assume an isothermal flow with sound speed c_s , which is reasonable for an AGB circumstellar envelopes beyond the wind acceleration zone. Here, Φ_{comp} is the gravitational potential of the companion in a circular motion. The companion is assumed to be a main-sequence star without mass loss. The effective potential Φ_p^{eff} represents the gravitational potential of the mass losing star $-GM_p/r$, but it also includes a term f/r to approximate the effect of stellar radiation pressure

¹Strictly speaking, the distance r should be replaced by the distance from the star, $(r^2 + r_p^2 - 2r_p r \sin \theta \cos(\phi - \phi_p))^{1/2}$, where r_p and ϕ_p refer the orbital radius of the mass losing star and the azimuthal angle in the orbit, respectively.

on dust as a wind acceleration mechanism. We have carried out several simulations with different values of f to clarify that the wind acceleration does not affect our results as far as the wind can escape. For the models presented in this paper (Table 1), $f = 1$ is employed so that the gas motion is only governed by the boundary condition at the surface of the mass losing star, the gravitational field of the companion, and the pressure gradient in the flow. Alternatively, this setup can be interpreted as that the wind is fully accelerated at the numerical surface of the mass losing star (2 AU from the star). In Table 1, all parameters with a subscript ‘ p ’ denote the quantities related to the mass losing star, e.g., the orbital radius of the mass losing star is r_p . The quantities for the companion star are denoted by a subscript ‘comp’. The subscript ‘ w ’ refers to the stellar wind mass loss from the primary star.

In order to compare the resulting structure with the corresponding single star case, we define the background as follows. We have carried out the same simulation with the individual model by placing the mass losing star at distance r_p from the center, but without introducing the orbital motion. The background density $\rho_0(r)$ and velocity $V_{w,0}(r)$ are defined as the averaged values over the azimuthal direction at distance r for the steady distribution about the single star located at r_p . By calculating the average values, we match the position of the star between the cases that the star is single and in a binary system. The notations with a subscript ‘0’ defined as above are technically different from S94’s notations with a superscript ‘ r ’ as measured in the rest frame of the mass losing star. However, the differences are negligible when the pattern of interest is located at a large distance from the star.

We first examine the anisotropic properties of wind material (or circumstellar envelope) purely due to the reflex motion of the mass losing star, by excluding the direct influence of companion’s gravitational potential (i.e., $\vec{\nabla}\Phi_{\text{comp}} = 0$) in most of models (M1–M6 in Table 1). For these models, only the indirect contribution of the companion causing the motion of the mass losing star is taken into account, which is analogous to S94 except for the inclusion of gas pressure and parcel interaction in the present study. We include the companion’s gravitational potential in model M7 to compare with results of model M6. The interpretation of the results from model M7 are based on the results found from models M1–M6 as well as results based on patterns solely due to the companion (gravitational density wake; see KT12).

4. RESULTS

To provide an overview of the structures resulting from the hydrodynamic simulations, a comparison of two models corresponding to different orbital speeds are presented. The cases for subsonic ($\mathcal{M}_p = 0.8$; model M1) and supersonic ($\mathcal{M}_p = 3.0$; model M2) orbital motion of the mass losing star are illustrated in Figures 2 and 3, respectively. Individual panels show (a) a single-armed spiral in the orbital plane, (b) circular arcs in a meridional plane, (c) fluctuations in the velocity profile along the distance from the system center, and (d) deviations of the density profile from the background $\sim r^{-2}$ density distribution.

A slow orbital motion of the mass losing star is expected to only slightly modify the gas flow pattern as a given parcel of the wind would not interact with other parcels. This suggests that the resultant wind properties would be analogous to S94’s diagnostics, except for the effect of gas pressure. Figure 2(c) indeed shows that the wind velocity varies between $V_{w,0}(1 \pm \beta_0)$ (long dashed lines) confirming the previous work by S94². The density profile in Figure 2(d) smoothly varies with a constant enhancement ratio (limited by the dot-dot-dot dashed lines), retaining a description as a power law with distance r from the orbital center (roughly -2) as ρ_0 .

In the case that the orbital motion is supersonic (model M2), however, the variations in the velocity and density profiles (Figure 3(c)–(d)) significantly decrease with distance in the orbital plane. This is likely due to the fact that wind parcels with different velocities, emerging at different times, bunch up and create a shock. In particular, it is seen that the peak velocities at the shock fronts level off after the first shock encounter.

4.1. Wind Velocity

Based on additional model computations for the subsonic motion of the mass losing star, it is found that the ratio of the orbital speed of the star to the intrinsic wind speed, as S94 suggested, is a good indicator for the magnitude of the velocity fluctuation, $(V_w - V_{w,0})/V_{w,0}$. However, in supersonic cases, this velocity ratio is not the best indicator for the variation in velocity profile. Specifically, the velocity for the wind parcel moving along the z -axis shows approximately constant excess as a function of distance as compared to S94’s expectation³.

We find that a revised velocity ratio defined by $\beta_0 = V_p/(V_{w,0} + c_s)$ matches the wind velocity for the parcel moving along the z -axis (cyan-colored line in Figure 3(c)) when used with S94’s corresponding formula (short dashed line; $V_w(z) = V_{w,0}(1 - \beta_0^2)^{1/2}$). Including the sound speed term in the definition of β_0 reduces the mean absolute deviation of the velocity difference from the formula for the wind parcel along the z -axis to 0.013% and 2.6% for M1 and M2 models, which are considerably smaller than the corresponding values without c_s (0.034% and 9.7%, respectively). For the subsonic model M1, the deviations from S94’s formulas for the azimuthal maximum and minimum velocities in the orbital plane are also reduced to 2.4% and 5.1% (from 4.9% and 7.2%).

In model M2 (Figure 3(c)), the wind velocity at the first shock position matches with S94’s formula for the maximum wind velocity. However, after encountering the first shock, the variation in wind flow speed is reduced, i.e., the maximum speed at a distance is smaller, and the minimum speed is larger, than the prediction based on the simple analysis of S94.

²The definition of $\beta_0 = V_p/(V_{w,0} + c_s)$ in this paper is slightly different from S94’s definition for $\beta' = V_p/V'_w$ without c_s . See Section 4.1.

³In S94, the orbital motion of the mass losing star modifies the velocity of the wind parcel moving along the z -axis to be $V_w = V'_w(1 - \beta'^2)^{1/2}$ where $\beta' = V_p/V'_w$.

We point out that the wind velocities vary in a binary system depending on the direction as shown in, for example, Figure 3(c). Here, the maximum velocity is $\sim 6.7 \text{ km s}^{-1}$ in the orbital plane, but $< 4.5 \text{ km s}^{-1}$ along the orbital axis, implying that the line-of-sight expansion velocity (usually determined by half spectral line width of molecular line emission) does not necessarily determine the pattern spacing appearing in the plane of the sky. Furthermore, this velocity (after modulated by the orbital motion of the binary system) is larger than that in the intrinsic wind model (dotted line; $< 5 \text{ km s}^{-1}$), which could be considered as mimicking a wind acceleration mechanism.

Finally, the variation of the maximum velocity (see above) with latitude also implies that the spectral line width can differ between an edge-on and (high angular resolution) face-on observation. A low resolution face-on observation will have a spectral line width between the values expected from the maximum velocities of the wind elements flowing through the orbital plane and along the orbital axis, representing the projected velocities of the flows over the entire envelope. However, a high angular resolution observation using an interferometer can resolve the central part, which in the case of a face-on view, corresponds to the flow along the orbital axis. The differing spectral line width in the central part may indicate the flow variation due to the (undetected) binary companion.

4.2. Density Profile

As the density contrast of the pattern can provide a diagnostic for the binary orbital parameters, we have illustrated in the last panel of each figure (2(d) and 3(d)), the density profile as a function of the distance from the center along $+x$ (red), $-y$ (yellow), $-x$ (green), and $+y$ (blue) in the orbital plane as well as along the orbital axis ($\pm z$; cyan).

To quantify the overall density distribution as a function of distance, the average density profile is defined as the average value of the density over all directions in the orbital plane at each distance. From all the simulated models, we find that the average density profile is the same as the intrinsic density profile (ρ_0 ; dotted) in both slope and magnitude, except for a slight deviation in the central region.

The density profile along the orbital axis (cyan) also preserves the value of ρ_0 except in models M2 and M3, which have the largest value of β_0 (i.e., $V_p/(V_{w,0} + c_s)$). In these models with fast orbital motions in a slow wind, the circumstellar envelopes are rarefied along the axis with shallower profiles, relative to the isotropic density of the corresponding single mass losing star (ρ_0). We note that since ρ_0 corresponds to the average density profile in the orbital plane, an ideal edge-on observation may show a deviation in density profiles depending on the direction angle from the orbital axis.

To quantify the maximum and minimum densities over all directions in the orbital plane, we make use of the numerical results displayed in Figure 2(d) for a subsonic orbital motion of the mass losing star (model M1). The density profiles along the five different directions (in color) are confined between $\rho_0(1 + \mathcal{M}_p)$ and $\rho_0(1 + \mathcal{M}_p)^{-1}$ (upper and lower dot-dot-dot dashed lines, respectively).

The density contrast, ρ_{\max}/ρ_{\min} , is thus $(1 + \mathcal{M}_p)^2$ at all distances (i.e., 3.24 for model M1).

On the other hand, the density profiles for the case of supersonic orbital motion (model M2) are displayed in Figure 3(d) showing significant deviation from the dot-dot-dot dashed curves. The deviation becomes larger with distance, particularly beyond $r/r_p \sim 16$, reducing the density contrast. This decrease of density contrast is also seen in Figure 4(d) for model M6 with a faster wind. This deviation is due to the peak densities forming a steeper profile than the average density profile (dotted), and the minimum density profile suddenly changes at $r/r_p \sim 130$. We note that the maximum and minimum density profiles eventually attain values given by $\rho_0(1 + \beta_0)$ and $\rho_0(1 + \beta_0)^{-1}$, respectively (long dashed lines).

A characteristic of the density profile is the existence of double peak features, which is best illustrated in Figure 3(d). For example, along $-x$ -axis (green line), the first arm extends between $r/r_p \sim 8$ and 12 bounded by sharp edges as hydrodynamic shocks. The second arm is found to exist between $r/r_p \sim 14.5$ and 26.5, again bounded by sharp edges. By comparing these two arms, one concludes that the arm width significantly increases in this model. The position of the outer edge is drawn by dashed lines in Figure 3(a)–(b), and the remaining density discontinuity traces the inner edge of the arm. Because of the shape (pitch angle) difference, the inner and outer edges overlap at around $+y$ -axis ($y/r_p \sim 16$), producing a thin sub-arm structure. The red line in Figure 3(d) has a tiny bump at $r/r_p \sim 19$ on top of the outer edge, and the green line shows a knee at $r/r_p \sim 22$ (also seen in the corresponding velocity profiles).

In the model with a faster wind (Figure 4), the double peaks are compressed by the fast wind so that they are not resolved as the density variations in the arm are small. However, the double peak feature is clearly seen in the velocity profiles. In particular, the red line in the density profile has a box shape with edges, for instance, at $r/r_p \sim 80$ and 100, corresponding to peaks in the velocity profile at $r/r_p \sim 80$ and 95. We note that the outer edge has a velocity peak at the density maximum, but that the inner velocity peak is located at the density minimum, which differentiates them.

The inner peaks in Figure 4(c) disappear beyond $r/r_p \sim 120$, where the minimum density values in Figure 4(d) suddenly jump to $\rho_0(1 + \beta_0)^{-1}$. A similar jump of density minima occurs in Figure 3(d) for the model M2 with a slow wind, but the density minima beyond $r/r_p \sim 16$ are still smaller than $\rho_0(1 + \beta_0)^{-1}$.

Eventually, the profiles of density maxima and minima in the models with supersonic orbital motion become steeper interior to the distance for the first overlap between inner and outer edges of the arm (Table 2), than for the density profile characteristic of a single mass losing star ($\sim r^{-2}$). We note that the average of the density over all azimuthal directions at a distance is nearly same with ρ_0 , despite the steeper profiles for maxima and minima. Beyond the overlap distance, the extrema may follow $\rho = \rho_0(1 + \beta_0)^{\pm 1}$ with $+$ and $-$ signs for the maxima and minima, respectively, resulting in a negligibly small density contrast.

4.3. Morphology

4.3.1. Pattern

The shape of the pattern in the outflowing wind is determined by the pattern propagation speed V_{pattern} in the radial direction. The spiral shape in the orbital plane can be expressed by the differential equation satisfying

$$\frac{d}{d(-\phi)} \left(\frac{r}{r_p} \right) = \frac{V_{\text{pattern}}}{V_p}. \quad (4)$$

Hence, measuring V_{pattern} is key in connecting the shape of the observed pattern to the orbital velocity V_p of the mass losing star. As shown in Figure 3(b), high density regions are bounded by circular shapes in a meridional plane. The dashed partial circles denote the outer boundaries of the enhanced density regions. By measuring the difference in position between adjacent circles, the pattern propagation speed averaged over one orbital period can be deduced.

Upon inspection of Figure 3(b), there is a systematic shift of the centers of the circles. This can be understood by simply tracing the locations of the wind parcels emerging at the same time. For a duration Δt , the individual wind parcels travel different distances, i.e., $(V'_w + V_p)\Delta t$ in the forward direction, $(V'_w - V_p)\Delta t$ in the backward direction, and $(V'^2_w - V_p^2)^{1/2}\Delta t$ in the lateral direction. Thus, the emerging parcels describe a circle about the center shifted by $V_p\Delta t$ with a radius of $V'_w\Delta t$ in a meridional plane. The resulting spiral pattern emerging in the orbital plane has an interval between arms given as $(V'_w + V_p) \times T_p$, where T_p is the orbital period. We note that this is only approximate because (1) a coordinate transformation is required from the frame comoving with the mass losing star to the observer's rest frame, (2) piling wind parcels with different velocities occurs, (3) $V_{w,0}$ is not exactly same with V'_w , and (4) gas pressure can affect the final configuration.

We decompose the pattern propagation speed as $V_{\text{pattern}} = V_{\text{radius}} + V_{\text{shift}}$ to distinguish the speeds corresponding to the center shift and the radius increase of the characteristic circles. The last four columns of Table 3 list V_{radius} and V_{shift} for the outer and inner circles as the boundaries of the excess density regions. Figure 5 illustrates our results in Table 3. The speeds corresponding to the increase of radius for the outer and inner circles, $V_{\text{out, radius}}$ and $V_{\text{int, radius}}$, respectively, show a good correlation with the average of the intrinsic wind speed (slightly better than the average of the resulting wind speed). The speeds for the outer circles are approximately the average wind speed, while the speeds for the inner circles are smaller by as much as $2c_s$. A fit to the 10 points results in a slope of 1.04 ± 0.03 . On the other hand, the centers of the circles shift with a speed proportional to the orbital velocity of the mass losing star. The speeds of the center shifts for the outer and inner circles are found to have a systematic difference of $0.5c_s$. Using the 10 points after correction of the systematic difference, a fit for the slope results in a value of 0.65 ± 0.03 . Therefore, we take the propagation speeds in the radial direction for the outer and inner boundaries of the pattern as

$$V_{\text{out}} = V_{w,0} + \frac{2}{3}V_p \quad (5)$$

and

$$V_{\text{int}} = (V_{w,0} - 2c_s) + \frac{2}{3} \left(V_p - \frac{1}{2}c_s \right), \quad (6)$$

respectively. The dashed lines in Figures 2(a)–(b), 3(a)–(b), and 4(a)–(b), based on Equation (5) combined with Equation (4), trace the density peaks at the outer edge of the pattern very well.

4.3.2. Standoff

The innermost region of the shock emanates from a position which we denote as the standoff distance. An estimate for this shock location is analogous to earlier work of Raga et al. (1990), who considered a one-dimensional accelerating jet in which one gas parcel can catch up the slower parcel ejected earlier. Since the required time for their encounter is the speed over the acceleration, the shock is located at a distance of $(\text{speed})^2/(\text{acceleration})$. Based on this concept, Raga et al. (2011) proposed a simple analytical model to explain the shock standoff distance from the mass losing star in circular motion under the action of the centripetal acceleration, V_p^2/r_p . In the rest frame of the mass losing star, however, the ejected wind is not only affected by the centrifugal acceleration in the radial direction, but also by the Coriolis acceleration ($V_p V_{w,0}/r_p$), perpendicular to the instantaneous direction of the wind parcel. Hence, obtaining the standoff distance is no longer a one-dimensional problem.

Nonetheless, we empirically find that this approach is a good approximation, as summarized in Table 4. In the second column of the table, the distance between the star and the first arm of the spiral pattern is listed. Here, we measure the distance to the shock in the direction opposite from the system center. In the cases that the wind and orbital speeds are comparable (models M2, M3, and M4), the shock standoff distance is comparable to Raga et al.’s prediction (third column in Table 4). However, for models M1, M5, and M6, in which the wind is much faster than the orbital speed, significant differences are present. A modified formula,

$$r_{\text{stand}}/r_p = \left(\frac{2 V_{w,0} + V_p}{3 V_p} \right)^2, \quad (7)$$

is found to represent the standoff distance for all simulated data sets.

4.3.3. Flattening

As described in Section 4.3.1, the positions for the density peaks in the meridional planes can be well traced by circular arcs. Furthermore, by comparing the structures displayed in Figure 2(b) and 3(b), it is evident that a higher orbital motion of the mass losing star causes the density distribution of the resulting circumstellar envelope to be more oblate-shaped. Here, we use the shape of the circular arcs to determine the overall vertical shape of the circumstellar envelope.

Using Equation (5), we define the eccentricity of the vertical shape as $e = (a^2 - b^2)^{1/2}/a$, where $a = V_{w,0} + 2V_p/3$ and $b = V_{w,0}$. The eccentricities for models M1–M6 are 0.42, 0.72, 0.81, 0.63, 0.43, and 0.47, showing that the model characterized by a relatively large orbital-to-wind velocity ratio (i.e., models M2–M4) has a more flattened shape. Hence, the overall eccentric shape of an observed pattern can be used to constrain the orbital velocity of the mass losing star with a given wind velocity.

Figure 6 exhibits another measure to quantify the flattening of the circumstellar envelope obtained by integrating the mass as a function of the angle from the orbital plane. For the fast orbital motion cases (M1–M3), the integrated mass normalized by the total mass shows a considerable systematic change with the orbital velocity of the mass losing star. This result indicates that the mass of the circumstellar envelope is concentrated toward the orbital plane, not just locally modulated within the pattern. This flattening is due to the action of the centrifugal force imparted to the gas by the motion of the mass losing star. As the models with faster winds (models M4–M6) follow the curve for a uniform density distribution, the flattening effect as a function of the orbital velocity is not distinguishable. We have also checked that its dependencies on other parameters such as the mass and orbital radius of the mass losing star are not significant.

Previously, Huggins et al. (2009) used the binary simulations of Mastrodemos & Morris (1999) to find that the flatness in the density distribution is determined by a single parameter, $GM_{\text{comp}}(r_p + r_{\text{comp}})^{-1}(V_w(r_{\text{comp}}))^{-2}$, with little dependence on $1 + q$ where $q = M_p/M_{\text{comp}}$. These results led them to conclude that the flattening of a circumstellar envelope in a binary system is caused by the gravitational focusing of the wind onto the companion. However, their first parameter can be rewritten as $(V_p/V_w)^2 \times (1 + q)$ using the binary mass ratio q factor. Given that the flattening is insensitive to q , we find that their flattening parameter can be simplified to $(V_p/V_w)^2$, which is consistent with the tendency found from our simulation results.

4.3.4. Inclination

The three-dimensional structure of the circumstellar envelope for a given model exhibits various shapes in the plane of the sky depending on the viewing inclination, from a spiral (0° ; face-on) to ring-like pattern (90° ; edge-on). For example, the case shown in Figure 7, corresponding to a model in which the orbital and wind velocities are comparable, reveals a peanut-shaped pattern when viewed edge-on because of the horizontal shifts of the ring-like pattern as described in Section 4.3.1.

The appearance of the patterns is spiral-like for a wide range of viewing angles, excluding angles very close to the edge-on ($\gtrsim 70^\circ$ – 80°). Previously, He (2007) pointed out that the majority of observed circumstellar patterns around evolved stellar binary systems will appear spiral-like. However, he only explored the case of a very fast wind compared to the orbital speed (the ratio greater than 10) in a simple piston model. Hence, the systematic elongation in the overall shapes

of the spirals was not found, which is prominent in, for example, our model M3 shown in Figure 7.

We also find that the elongated spirals in the mid-range of viewing inclinations are tilted. That is, the line connecting the longest axis of the elongated spiral in the plot for $i = 60^\circ$, for example, does not match with the $l = 0$ axis, which is the intersection of the viewing plane with the orbital plane. Here, the orientation of the tilt depends on the orientation of the orbital motion.

Figure 7 shows the density distribution in the mid plane in the line-of-sight direction, which dominates the central channel of a velocity channel map (see middle panel of Figure 8). In different velocity channels, however, the patterns exhibit different tilt orientations and angles. The middle row of Figure 8 demonstrates the channels close to the central velocity, reflecting the density distribution close to the mid plane. The longest axes of the patterns in these three panels are rotated counterclockwise from $l = 0$ axis. However, in the outer layers (or in higher velocity channels), the patterns are twisted and the longest axes are rotated in the clockwise direction. This trend reverses when the star orbits in the clockwise direction, opposite to the cases displayed here. It is also worth noting that the column density map does not show the mismatch of the axis of the pattern from the line of nodes since all the channels characterized by different degrees of mismatch are integrated out.

4.4. Effects of Companion Wake

In previous sections, we focused on the asymmetric pattern caused by the reflex motion of the mass losing star as a result of the indirect influence of the binary companion. In those models, we suppressed the direct effect of the companion, which assembles wind material to create a gravitational wake. In model M7, we include the influences of both stellar motions in modulating the circumstellar envelope around an evolved binary stellar system. By comparing this model with model M6, whose initial setup is the same as M7 except for the gravitational wake of the companion star, we separately investigate the direct and indirect effects due to a companion star.

The properties of a companion’s gravitational wake is described by KT12 in detail. In this previous work, the companion is assumed to be a substellar mass object in order to minimize the reflex motion of the mass losing star. Although the companion’s mass adopted in this paper is comparable to the AGB star, we show that the previous results can be applied in this case as well.

Similar to the pattern caused by the motion of the mass losing star, the gravitational wake of a companion described in KT12 exhibits a single-armed spiral in the orbital plane and a circular arc pattern in meridional planes. However, these two patterns have three differences, which complicate the resulting structures.

The first difference is that the companion’s wake is attached to the companion⁴, while the

⁴For a massive companion, the gravitational wake can be detached by up to distance of $GM_{\text{comp}}(V_{\text{comp}}^2 - c_s^2)^{-1}r_s^{-1}$

pattern due to the motion of the mass losing star stands off at the distance as in Equation (7). The second difference stems from the propagation speeds of the patterns determining the shape. For the companion’s wake, the centers of the arcs appearing in meridional planes are fixed at the orbital distance of the companion, i.e., $V_{\text{shift}} = 0$ (see for example Figure 1 of Kim 2011) and the radii of the arcs increase with speed $V_{\text{radius}} = V_w \pm c_s$, where the upper and lower signs correspond to the outer and inner edges of the regions of excess density, respectively (c.f., Equations (5)–(6)). Third, while the arc pattern due to the reflex motion of the mass losing star nearly reaches the orbital axis, the gravitational wake of the companion forms within a very limited height from the orbital plane, up to the angle of $\tan^{-1}((\mathcal{M}_{\text{comp}}^2 - 1)^{1/2}/(1 + 0.2\mathcal{M}_w\mathcal{M}_{\text{comp}}))$, that is Equation (13) from KT12.

In Figure 9(a)–(b), we present the shape of pattern in model M7 for the binary system, overlaid with the corresponding shape in model M6 excluding the gravitational wake of the companion (dashed lines). It is definitely seen that the pattern shape has contracted by including the direct effect of the companion. This difference arises due to the existence of a shock front producing a distinctive inner edge of the spiral arm structure in Figure 9(a), which was absent in Figure 4(a) without the companion’s wake.

The flow slows immediately after the spiral shock corresponding to the inner edge of the companion wake. For instance, the red line in Figure 9(c) for the fluid speed along $+x$ -axis drops at $r/r_p \sim 22$ and ~ 27 . In contrast, in Figure 4(c) without the companion wake, it decreases continuously in the range of $r/r_p \sim 24$ –29. Since the flow after the shock at $r/r_p \sim 22$ in model M7 is slower than in the case where the companion wake is not taken into account, the pattern propagation speed is decreased thus shrinking the pattern.

This shape discrepancy between the models with (M7) and without (M6) the gravitational wake of the companion is, however, insignificant at high latitudes as shown in Figure 9(b). This latitude dependence is related to the white solid lines in the figure, which indicates the vertical extension limit of the companion’s wake influence, from KT12. Indeed, one can easily find the clumpy structures within the limits, which is the wake of the companion. Since the shock associated with the companion’s wake does not exist at high latitudes, the wind can flow in a similar manner to the case excluding the companion’s wake effect.

The contribution of a companion’s wake to the structure due to the motion of the mass losing star is clearly seen in a zoomed image in Figure 10. The plots for inclinations $i > 0^\circ$ display clumpy structures due to the overlap of the companion’s wake, while for the face-on inclination a continuous, distinct inner edge of the spiral arm is seen. In the panel for $i = 30^\circ$, the wake of the companion presents a distinctive knot at $x/r_p \sim -8$ and a wiggly distribution on the opposite side connected by a spiral pattern due to the primary star’s reflex motion. It is worth noting that

in a static background (see Kim & Kim 2009; Kim 2010). However, this detachment hardly occurs in outflowing background because the material is swept out by the wind (KT12). Here, r_s is the gravitational softening radius of the object.

the spiral is patchy for an inclination $i = 60^\circ$. We emphasize that the knots do not represent the companion star and the spiral patterns in these inclinations are not the companion’s wake. The latter point is clarified by the corresponding column density in Figure 11, revealing that the knotty structures are indeed due to a superposition of two spiral patterns formed by the motions of the individual stars.

In contrast to the structure due to the reflex motion of the mass losing star, the wake of the companion star significantly changes its apparent shape as a function of the inclination angle (Figure 11). This is due to the fact that the companion wake is vertically thin, so that it closely corresponds to the orbital plane. Therefore, if the emission is sufficiently optically thin, but sensitive enough, to detect the companion wake, the viewing inclination angle may be inferred from the positional displacement between the two spiral-like structures.

From the black solid curve in Figure 9(d), we clarify that the density enhancement in the overlap regions with respect to the average density (calculated by $(\rho_{\max} - \rho_0)/\rho_0$) is consistent with a linear superposition of the amounts of density enhancements due to the two mechanisms. To account for the effect of reflex motion to the density enhancement in Figure 4(d), we have used a fitting formula (given in Table 2) for the maximum density enhancement as a function of distance. For the calculation of the density enhancement in the gravitational wake of the companion, we have taken the formula⁵ empirically found in KT12. The summation of these enhancement values (black solid line in the figure) matches very well with the maxima of the density profiles (red, yellow, green, and blue colors) in the orbital plane of the binary system. The change in minimum densities from the values in Figure 4(d) is negligible (see Figures 5–6 in KT12).

5. DISCUSSION

As shown in the previous sections, the motion of the components in a binary system can generate various morphologies in the outflowing circumstellar envelopes of stars in the AGB phase. A detailed examination of the shape of the pattern, the density profile, and the kinematics can, in principle, provide constraints on the binary orbital properties. In the following, we apply our theoretical results to provide an interpretative framework of the large scale global properties of the observed asymmetric pattern in the circumstellar envelope of the carbon-rich AGB star AFGL 3068.

AFGL 3068 is one of the best test cases for investigation within the framework of the binary

⁵Equation (12) of KT12 is rewritten as

$$\delta\rho/\rho = \frac{GM_{\text{comp}}/c_s^2}{|r - r_{\text{comp}}|} \left(\frac{\frac{|r - r_{\text{comp}}|}{GM_{\text{comp}}/c_s^2} V_w^2 + 10V_w V_{\text{comp}} + c_s^2}{V_w^2 + |V_{\text{comp}}^2 - c_s^2|} \right)^{1/2}.$$

scenario since it possesses a well-defined spiral pattern extending over a large area of the circumstellar envelope. It is seen in optical wavelengths (Mauron & Huggins 2006, MH06 hereafter) as a result of the scattering by dust illuminated by Galactic light. Observational evidence exists for two point-like, near-infrared sources at the center (Morris et al. 2006) of the envelope with a projected separation of $0''.11$ (109 AU, assuming the distance of 1 kpc). Five turns of the spiral pattern are detected over $12''$ from the center ($\sim 10^4$ AU). MH06 used the spacing between spiral arms of $2''.29$ (2300 AU) to derive a binary orbital period of 830 yr, assuming that the observed spiral pattern propagates outward with the speed (14 km s^{-1}) taken as the expansion velocity of the envelope.

From Figure 8 of MH06, however, we find that their sketch of an Archimedes spiral mismatches with the position of peak intensity. The observed pattern is elongated in the northwest-southeast direction. The ratio between the longest axis of the observed pattern and the length perpendicular to this axis is found to be 1.1. Considering that the appearance of the pattern is unlikely in an edge-on view, the ratio in the edge-on view (or the aspect ratio of the oblate spheroid) must be larger ($a/b \geq 1.1$). The corresponding eccentricity ($e \geq 0.42$) is consistent with M4–M6 models, which correspond to the cases for an orbital velocity greater than 2.2 km s^{-1} with a similar wind velocity. Using the analysis in Section 4.3.3, we obtain the velocity ratio of $V_p/V_{w,0} \geq 0.15$.

An additional constraint on the orbital velocity of the mass losing star is found from the maximum line-of-sight velocity of 14 km s^{-1} . As seen in Figures 2(c), 3(c), 4(c), and 9(c), the wind velocity cannot exceed $V_{w,0} + V_p$ in any direction, thus $V_{w,0} + V_p \gtrsim 14 \text{ km s}^{-1}$. This velocity is not likely to be very different from 14 km s^{-1} . Combining this with the constraint derived from the eccentricity of the overall shape of the pattern yields $V_p \gtrsim 1.8 \text{ km s}^{-1}$ and $V_{w,0}$ close to 12.2 km s^{-1} . Models M4 and M5 satisfy the conditions for the wind and orbital velocities.

The pattern spacing of $2''.29$ with the corrected pattern propagation speed of $V_{w,0} + 2V_p/3$ yields an orbital period T_p of about 820 yr, which is not significantly different from MH06’s result. The corresponding orbital radius of the mass losing star is $r_p \geq 0''.050$ or 50 AU. Comparing this value with the *projected* binary separation of 109 AU (Morris et al. 2006) implies that either the binary mass ratio $q = M_p/M_{\text{comp}}$ corresponding to r_{comp}/r_p is small (possibly less than 1) or the projection effect is significant (i.e., high inclination). With the binary separation of ≥ 109 AU and the derived limit of the orbital velocity $V_p \gtrsim 1.8 \text{ km s}^{-1}$, the binary mass ratio is constrained to be⁶ $q \lesssim 2.5$ – 2.9 , adopting the mass of a carbon star as $M_p \leq 3$ – $4 M_{\odot}$ assuming such stars do not undergo the hot bottom burning process (García-Hernández et al. 2006, and references therein).

The arm width of $\lesssim 0''.5$ reported in MH06 can also be used to infer a property of the circumstellar envelope when compared with the theoretical distance of double peaks (inner and outer edges of the arm). Equations (5)–(6) indicate that the arm width corresponds to $2.34c_s \times T_p$, implying a sound speed $c_s \lesssim 1.2 \text{ km s}^{-1}$ or temperature less than 150 K, if $T_p = 820$ yr. We note that our M4 model assumes a sound speed of 1 km s^{-1} , which is in the range estimated from the observed

⁶It is calculated by $V_p^2 r_p^{-1} = GM_{\text{comp}}(r + r_{\text{comp}})^{-2}$, or equivalently $q(1+q) = GM_p(r_p + r_{\text{comp}})^{-1} V_p^{-2} \lesssim 8.5$ – 11.3 .

arm width. The velocity spread corresponding to broadening of the arm width ($2.34c_s$) is small compared to the pattern propagation speeds for the outer and inner peaks, which prevents the overlap of the outer and inner peaks in the region where the scattered light is detected. However, molecular line observations indicate that the temperature of the circumstellar envelope is plausibly much lower than 150 K at the distance where the spiral pattern is detected (10–30 K, Woods et al. 2003). The difference in temperature may imply that the arm width is not fully resolved within $0''.5$ or that our assumption of isothermality breaks down. Given that the isothermal assumption provides a very good description of the overall shape of the pattern, the broadening of the arm width may be caused by a local temperature increase within the shocked spiral arm.

In a separate paper, Kim & Taam (2012b) modeled the circumstellar envelope of AFGL 3068 using an adiabatic equation of state with the specific heat ratio of 1.4. The calculations show that the temperatures in the shocked arm are as high as 1000 K. In the range of arm temperatures (~ 100 – 1000 K), the heating timescale due to the gas-dust collisions in the postshock region for $0.1 \mu\text{m}$ -sized grains is similar to (or slightly smaller than) the timescale for cooling via molecular line transitions (Edgar et al. 2008), indicating that the adiabatic equation of state without including the above heating and cooling mechanisms should be reasonable. Here, we note the important point that the spiral shape for a non-isothermal gas is as predicted in Equation (5) of the current work.

Finally, we compare the theoretical prediction for the density contrast with the value estimated from the observations. From the intensity jump of a factor of up to ~ 2.5 , MH06 derived the density contrast corresponding to a factor of up to ~ 5 assuming a nested shell model. In comparison, our spiral model predicts a density contrast up to $\sim (1 + \mathcal{M}_p)^2 \gtrsim 6$ with $V_p \gtrsim 1.8 \text{ km s}^{-1}$ and $c_s \lesssim 1.2 \text{ km s}^{-1}$. The contrast decreases with increasing distance from the center, as low as $(1 + \beta_0)^2$ (a level of 1.3) beyond the distance where overlap of the inner and outer shocks occurs. The contrast in the observed intensity profile may correspond to the contrast of column density if the scattering is optically thin. We note that the first arm in model M4 is characterized by a column density contrast of a factor of 2–7 and the volume density contrast as high as a factor of a few tens, depending on the distance from the center as well as the choice of the reference value.

6. SUMMARY AND CONCLUSION

We have carried out three dimensional hydrodynamic simulations to investigate the effects of a companion to an AGB star in a binary system to understand the physics and kinematics of the observed asymmetric patterns in outflowing circumstellar envelopes. It is found that the reflex motion of the mass losing star, due to the indirect effect of the companion, dominates the overall structure of the circumstellar envelope. The direct effect associated with the gravitational wake of the companion results in a similar, but narrower pattern, imprinted on the broader spiral pattern. The overlaps of the two patterns result in the generation of clumpy structures. The appearance of these structures, as well as the spiral-like pattern, is evident for a wide range of inclination angles. By extending the study to include cases for a slow wind, we find a systematic flattening

of the spiral-like pattern with the viewing inclination. A quantitative description of the flattening is presented in terms of a ratio between the wind and orbital velocities. In particular, constraints on the orbital speed of the mass losing star as well as the inclination angle of the system (from the flattening of the overall shape and the deviation of the detailed pattern from a spiral) can, in principle, be obtained. However, a high sensitivity/resolution observation is required to trace the full spiral pattern, given that the inclined spirals are possibly patchy. Additional constraints on the system can be obtained from the amplitudes of the density and velocity modulations as compared to those characteristic for a single mass losing star. The numerical results have been applied to the extreme carbon star AFGL 3068, and we find that the physical parameters are within reasonable ranges for circumstellar envelopes.

Although our model comparison is consistent with the observed pattern shape and density contrast of AFGL 3068, several aspects can be improved in future work. For example, the observed arm width is thin compared to the modeled column density distribution, perhaps, implying that the sound speed is less than 1 km s^{-1} . In addition, the applied model does not match the small scale details, for which fine tuning of the model is required. Inclusion of the gravitational wake of the companion will be necessary as the companion mass sensitively affects the small scale details as well as the mass ratio in determining most of the orbital parameters in a binary system. Finally, the possibility of eccentric orbits should be considered as the departure from circular motion may modify the fine structures as suggested by He (2007) in a simple ballistic model.

We are grateful to the anonymous referee and Dr. N. Mauron for their fruitful comments which helped to increase the significance and potential of this work. This research is supported by the Theoretical Institute for Advanced Research in Astrophysics (TIARA) in the Academia Sinica Institute of Astronomy and Astrophysics (ASIAA). The computations presented here have been performed through the ASIAA/TIARA computing resource, using FLASH3.0 code developed by the DOE-supported ASC/Alliance Center for Astrophysical Thermonuclear Flashes at the University of Chicago.

REFERENCES

- Balick, B., & Frank, A. 2002, *ARA&A*, 40, 439
- Bondi, H. 1952, *MNRAS*, 112, 195
- Bondi, H., & Hoyle, F. 1944, *MNRAS*, 104, 273
- Castro-Carrizo, A., Quintana-Lacaci, G., Neri, R., et al. 2010, *A&A*, 523, A59
- Darwin, G. H. 1879, *Proceedings of the Royal Society of London*, 29, 168
- Decin, L., Royer, P., Cox, N. L. J., et al. 2011, *A&A*, 534, A1

- De Marco, O. 2009, *PASP*, 121, 316
- de Val-Borro, M., Karovska, M., & Sasselov, D. 2009, *ApJ*, 700, 1148
- Dinh-V.-Trung, & Lim, J. 2009, *ApJ*, 701, 292
- Edgar, R. G., Nordhaus, J., Blackman, E. G., & Frank, A. 2008, *ApJ*, 675, L101
- Fong, D., Meixner, M., Sutton, E. C., Zalucha, A., & Welch, W. J. 2006, *ApJ*, 652, 1626
- García-Hernández, D. A., García-Lario, P., Plez, B., et al. 2006, *Science*, 314, 1751
- He, J. H. 2007, *A&A*, 467, 1081
- Hoyle, F., & Lyttleton, R. A. 1939, *Proceedings of the Cambridge Philosophical Society*, 34, 405
- Huggins, P. J. 2007, *ApJ*, 663, 342
- Huggins, P. J., Mauron, N., & Wirth, E. A. 2009, *MNRAS*, 396, 1805
- Iben, I., Jr., & Livio, M. 1993, *PASP*, 105, 1373
- Johnson, J. J., & Jones, T. J. 1991, *AJ*, 101, 1735
- Kim, H. 2011, *ApJ*, 739, 102
- Kim, H., & Kim, W.-T. 2009, *ApJ*, 703, 1278
- Kim, H., & Taam, R. E. 2012a, *ApJ*, 744, 136 (KT12)
- Kim, H., & Taam, R. E. 2012b, *ApJ*, submitted
- Kim, W.-T. 2010, *ApJ*, 725, 1069
- Mastrodemos, N., & Morris, M. 1999, *ApJ*, 523, 357
- Mauron, N., & Huggins, P. J. 2006, *A&A*, 452, 257 (MH06)
- Mayer, A., Jorissen, A., Kerschbaum, F., et al. 2011, *A&A*, 531, L4
- Miszalski, B., Acker, A., Parker, Q. A., & Moffat, A. F. J. 2009, *A&A*, 505, 249
- Mohamed, S., & Podsiadlowski, P. 2011, *Why Galaxies Care about AGB Stars II: Shining Examples and Common Inhabitants*, 445, 355
- Morris, M. 1987, *PASP*, 99, 1115
- Morris, M., Sahai, R., Matthews, K., Cheng, J., Lu, J., Claussen, M., & Sánchez-Contreras, C. 2006, *Planetary Nebulae in our Galaxy and Beyond*, 234, 469

- Neri, R., Kahane, C., Lucas, R., Bujarrabal, V., & Loup, C. 1998, *A&AS*, 130, 1
- Nordhaus, J., & Blackman, E. G. 2006, *MNRAS*, 370, 2004
- Nordhaus, J., Spiegel, D. S., Ibgui, L., Goodman, J., & Burrows, A. 2010, *MNRAS*, 408, 631
- Pascoli, G., & Lahoche, L. 2010, *PASP*, 122, 1334
- Raga, A. C., Binette, L., Canto, J., & Calvet, N. 1990, *ApJ*, 364, 601
- Raga, A. C., Cantó, J., Esquivel, A., Huggins, P. J., & Mauron, N. 2011, in *Asymmetric Planetary Nebulae 5 Conference*, ed. A. A. Zijlstra, F. Lykou, I. McDonald, and E. Lagadec (Jodrell Bank Centre for Astrophysics, Manchester), 185
- Raghavan, D., McAlister, H. A., Henry, T. J., et al. 2010, *ApJS*, 190, 1
- Schmidt, G. D., Hines, D. C., & Swift, S. 2002, *ApJ*, 576, 429
- Soker, N. 1994, *MNRAS*, 270, 774 (S94)
- Soker, N. 1996, *ApJ*, 460, L53
- Taam, R. E., & Sandquist, E. L. 2000, *ARA&A*, 38, 113
- Theuns, T., & Jorissen, A. 1993, *MNRAS*, 265, 946
- Trammell, S. R., Dinerstein, H. L., & Goodrich, R. W. 1994, *AJ*, 108, 984
- van Winckel, H. 2003, *ARA&A*, 41, 391
- Winters, J. M., Le Bertre, T., Jeong, K. S., Helling, C., & Sedlmayr, E. 2000, *A&A*, 361, 641
- Woods, P. M., Schöier, F. L., Nyman, L.-Å., & Olofsson, H. 2003, *A&A*, 402, 617

Table 1. Parameters for hydrodynamic simulations

Model	Properties of Binary System				Domain Information		
	V_p [km s ⁻¹]	V'_w @ r_* [km s ⁻¹] ([AU])	c_s [km s ⁻¹]	$M_p/M_{\text{comp}}^\dagger$	L [AU]	ΔL [AU]	refinement [‡]
M1	0.8	0.1 (2)	1	(4.6)	1600	0.2 – 12.5	9 – 3
M2	3.0	0.1 (2)	1	(1.5)	400	0.2 – 3.13	7 – 3
M3	5.0	0.1 (2)	1	(1.0)	400	0.2 – 3.13	7 – 3
M4	4.7	10. (2)	1	(1.0)	1600	0.2 – 12.5	9 – 3
M5	2.2	10. (2)	2	(2.0)	1600	0.2 – 12.5	9 – 3
M6	2.2	10. (2)	1	(2.0)	1600	0.2 – 12.5	9 – 3
M7	2.2	10. (2)	1	2.0	1600	0.2 – 12.5	9 – 3

Note. — Each column represents [1] model name, [2] orbital speed of the mass losing star, [3] wind launching speed on the stellar surface, defined by the boundary of the resetting radius (r_*), [4] isothermal sound speed, [5] mass ratio between the mass losing star and the companion, [6] half of domain size, [7] range of spatial resolution, and [8] corresponding range of refinement level with the mother grids of $64 \times 64 \times 32$ in (x, y, z) -directions. Mass M_p , mass loss rate \dot{M}_p , and orbital radius r_p of the mass losing star are $1 M_\odot$, $10^{-6} M_\odot \text{yr}^{-1}$, and 10 AU, respectively.

[†]Direct effect of the gravitational potential of the companion is included only in model M7. In the other models, the companion’s gravitational wake is suppressed so that the only role of companion is to cause the mass losing star to orbit around the center of mass.

[‡]Static, centrally concentric mesh is employed.

Table 2. Maximum density profile

Model	ρ_{\max}		$(\rho_{\max} - \rho_0)/\rho_0$	
	$a \times 10^{14}$	n	a	n
M1	1.2	−2.3	5.1	−0.5
M2	2.5	−2.5	13	−0.7
M3	4.8	−2.8	33	−1.0
M4	6.8	−3.3	1100	−1.8
M5	0.39	−2.6	120	−1.1
M6	5.4	−3.1	2300	−1.7

Note. — $f(r) = a(r/r_p)^n$ is taken for the fitting functional form. For all models, the slope of the mean density profile is measured to be in the range of -2.0 to -2.2 depending on distance from the orbital center.

Table 3. Pattern propagation speed

Model	V_p	$\langle V_{w,0} \rangle$	$\langle V_w \rangle$	$\Delta(\text{radius})/T_p$		$\Delta(\text{shift})/T_p$	
				outer	inner	outer	inner
M1	0.8	5.2	5.3				
M2	3.0	4.7	5.2	5.1	1.8	2.1	1.8
M3	5.0	4.7	6.3	5.4	3.3	3.0	2.7
M4	4.7	11.	12.	11.	8.6	3.2	3.0
M5	2.2	14.	14.	15.	12.	1.1	0.4
M6	2.2	11.	11.	11.	9.9	1.4	1.0

Note. — Each column represents [1] model name, [2] orbital velocity of the mass losing star, [3] average of the intrinsic wind velocity in the orbital plane over the simulated domain, [4] average of the resulting wind velocity in the orbital plane over the simulated domain, [5] and [6] increases of the radii of circles in (x, z) plane for the outer and inner boundaries of the high density regions, respectively, and [7] and [8] increases of the shifts of the centers of the circles. Here, T_p represents the orbital period.

Table 4. Standoff distance

Model	r_{stand}/r_p	$\langle V_{w,0} \rangle / V_p)^2$	$(0.66 \langle V_{w,0} \rangle + V_p)/V_p)^2$
M1 [†]	21.	42.	25.
M2	2.5	2.5	3.0
M3	1.4	0.9	1.7
M4	4.9	5.6	5.0
M5 [†]	22.	39.	23.
M6	18.	25.	16.

[†]Because M1 and M5 models do not have definitely defined shock features, we choose the position showing relatively high density gradient.

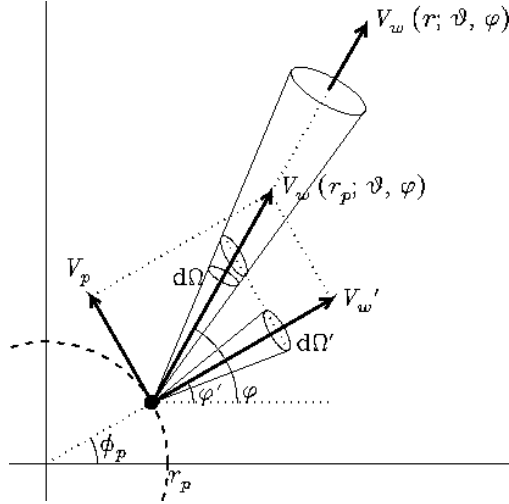


Fig. 1.— Schematic diagram illustrating the modification of wind geometry due to the orbital motion of the mass losing star in a binary system. The mass losing star is located at $(r, \theta, \phi) = (r_p, \pi/2, \phi_p)$, marked by a filled circle, and orbiting on the dashed circle. Its wind velocity \vec{V}_w in the center of mass frame is determined by the vector sum of the intrinsic wind velocity \vec{V}'_w , which is the velocity in the frame of the mass losing star, with the orbital velocity of the star \vec{V}_p . The solid angle of a wind parcel is consequentially modified to $d\Omega = S d\Omega'$. See text (and S94) for details of the projection factor S . The directions of velocity vectors are defined by the spherical coordinate angles ϑ and φ about the position of the mass losing star.

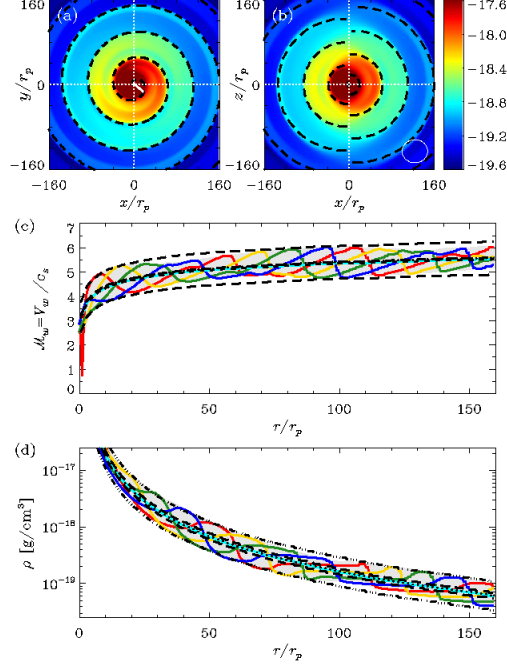


Fig. 2.— Model M1 for a subsonic orbital motion ($\mathcal{M}_p = 0.8$) of the mass losing star. The density distributions (a) in the orbital plane and (b) in a meridional plane are coded in a logarithmic color scale as labeled in the color bar. The dashed lines outlining the spiral pattern in (a) and the circular arc pattern in (b) are drawn based on the empirical formulae in Section 4.3.1. In (a), the white straight line from the center shows the standoff distance of the spiral pattern, described in Section 4.3.2. At the bottom right corner of (b), the ellipse displays the overall shape in meridional planes (see Section 4.3.3). (c) The total velocity profiles of wind flow in the unit of sound speed c_s as a function of distance from the orbital center in $+x$ (red), $-y$ (yellow), $-x$ (green), and $+y$ (blue) directions show variation between $\mathcal{M}_{w,0}(1 \pm \beta_0)$ (top and bottom long dashed), where $\mathcal{M}_{w,0}$ and \mathcal{M}_p refer the Mach numbers of the intrinsic wind motion (dotted) and the orbital motion, respectively. Middle long dashed line displays the Mach number averaged over azimuthal direction. The wind flowing along the orbital axis (cyan) has the predicted speed $\mathcal{M}_w(z) = \mathcal{M}_{w,0}(1 - \beta_0^2)^{1/2}$ (short dashed) where $\beta_0 = \mathcal{M}_p/(\mathcal{M}_{w,0} + 1)$. (d) The corresponding density profiles (red, yellow, green, blue, and cyan colors) are located between the dot-dot-dot-dashed lines indicating $\rho = \rho_0(1 + \mathcal{M}_p)^{\pm 1}$, where ρ_0 (dotted) fits with the average density profile. For comparison, long dashed lines show the profiles for $\rho = \rho_0(1 + \beta_0)^{\pm 1}$. All the lengths are scaled by the orbital radius r_p of the mass losing star.

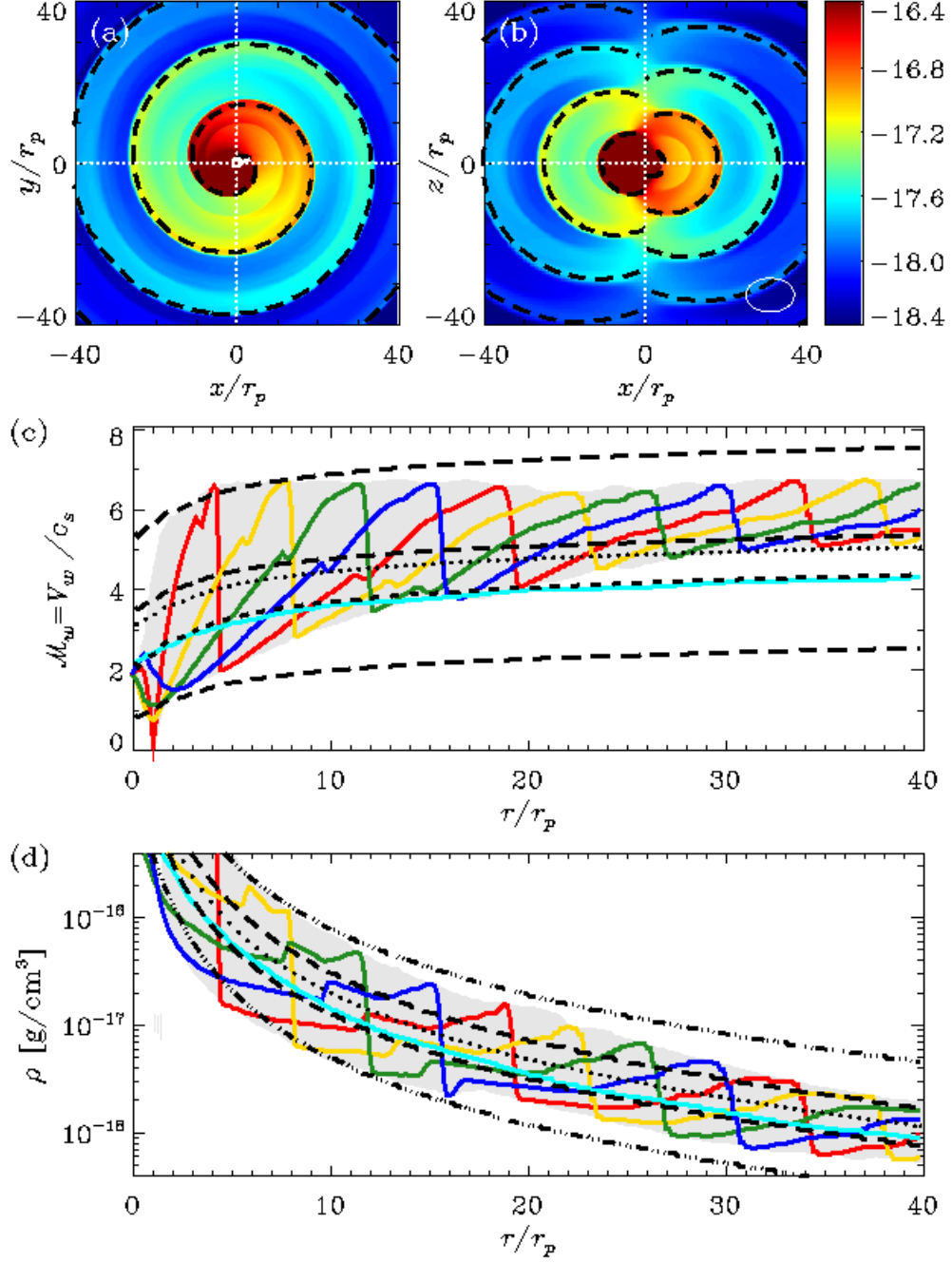


Fig. 3.— Model M2 for a supersonic orbital motion ($\mathcal{M}_p = 3.0$) of the mass losing star. See Figure 2 for the details.

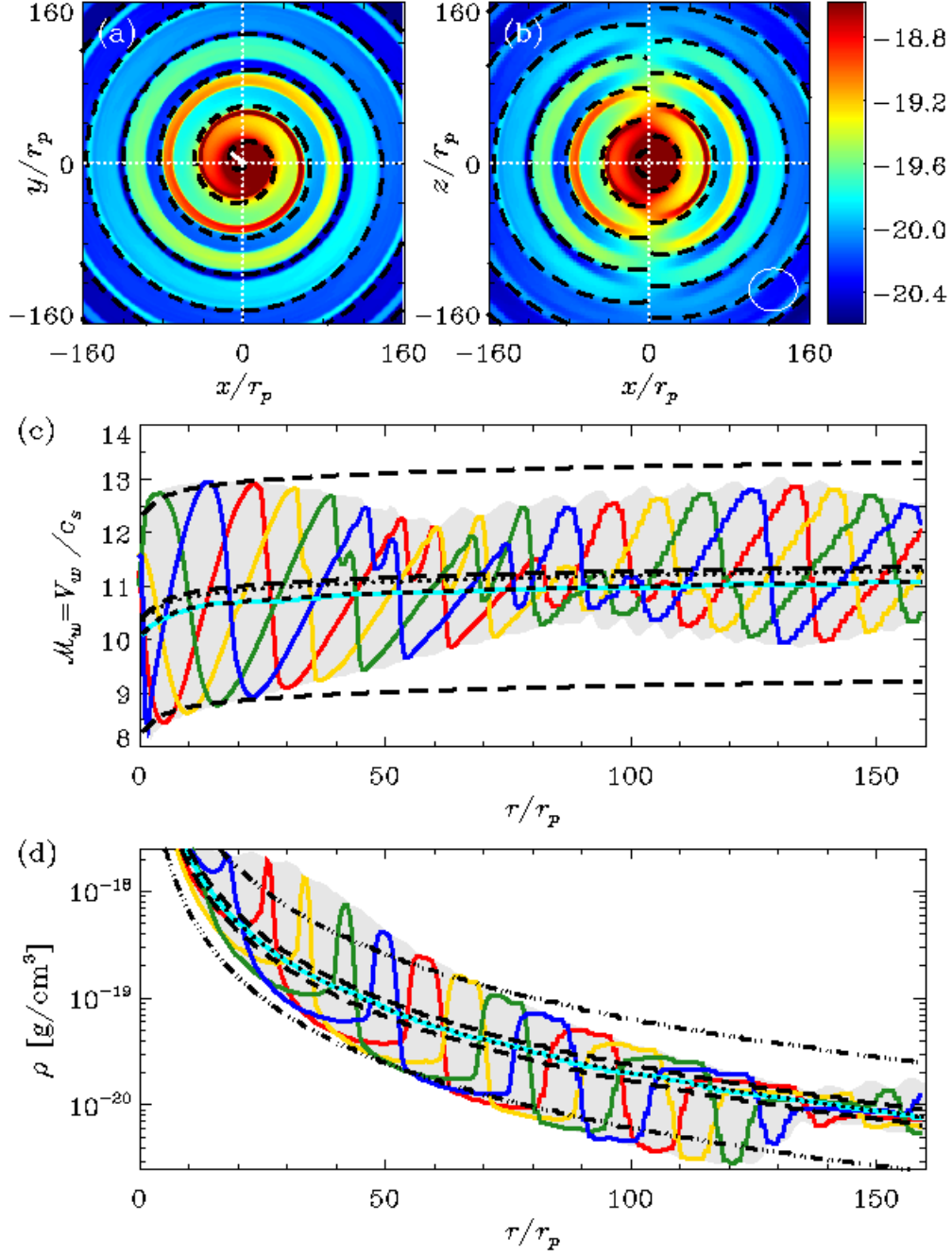


Fig. 4.— Same as Figures 2 and 3, but for model M6 with a faster wind ($\mathcal{M}_w \sim 10$). See Figure 2 for the details.

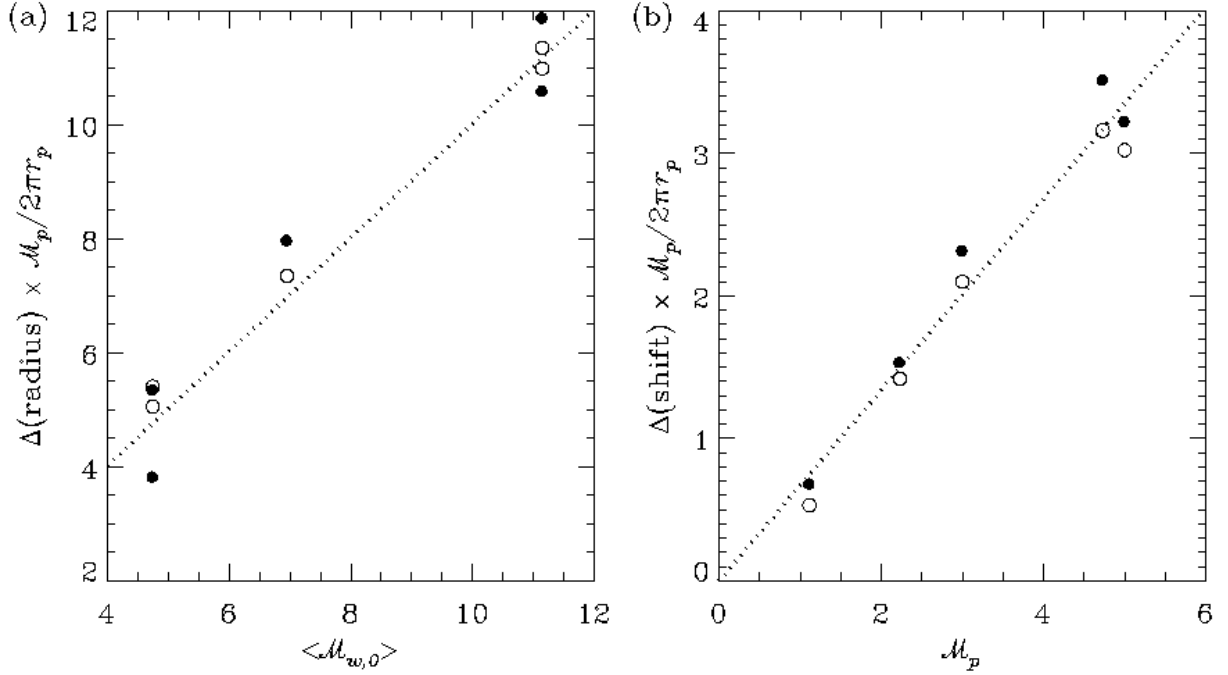


Fig. 5.— The pattern propagation speed for M2–M6 models in Mach number in the radial direction decomposed to two parts, $\mathcal{M}_{\text{radius}}$ and $\mathcal{M}_{\text{shift}}$, relevant to the circular shapes found in meridional planes. (a) $\mathcal{M}_{\text{out, radius}}$ (open symbols) and $\mathcal{M}_{\text{int, radius}} + 2$ (filled symbols) versus the average wind Mach numbers, $\langle \mathcal{M}_{w,0} \rangle$, follow the dotted line of slope 1. The linear fit for the slope of the 10 points is 1.04 ± 0.03 . (b) The centers of the circles shift with the speed proportional to the orbital speed. $\mathcal{M}_{\text{out, shift}}$ (open symbols) and $\mathcal{M}_{\text{int, shift}} + 0.5$ (filled symbols) as a function of the orbital Mach number, \mathcal{M}_p , are linearly fitted with the slope of 0.65 ± 0.03 . The slope of the dotted line is $2/3$.

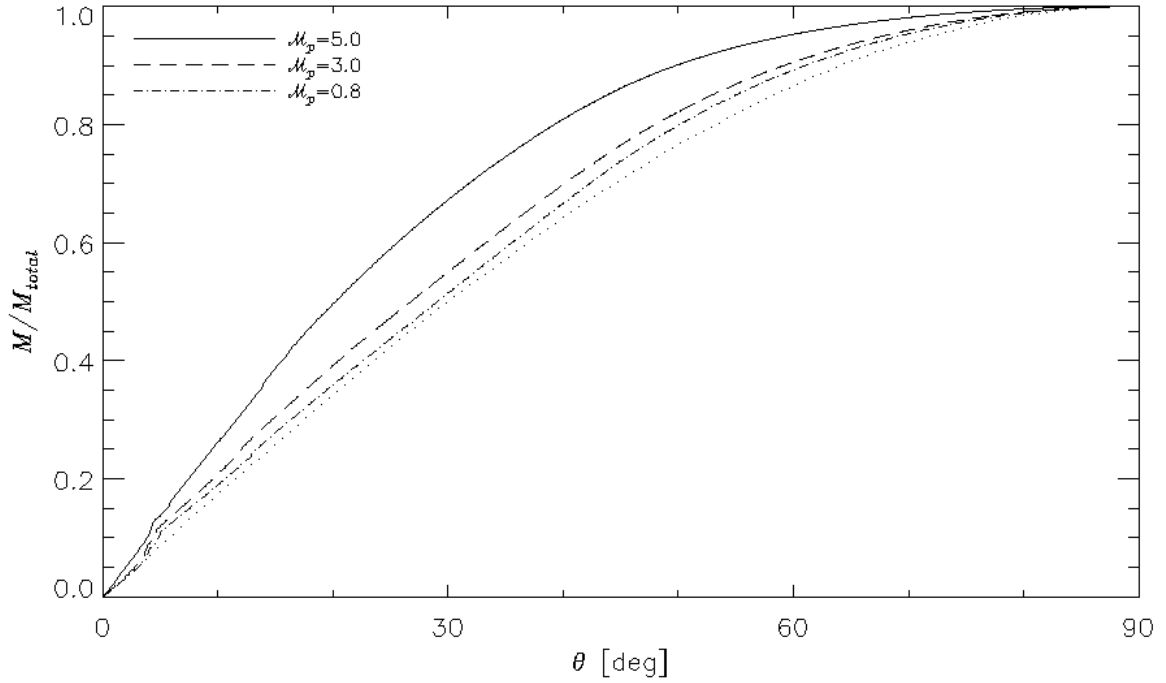


Fig. 6.— Integrated mass normalized by the total gas mass as a function of the latitudinal angle from the orbital plane. The models M1 ($\mathcal{M}_p = 0.8$; dot-dashed), M2 ($\mathcal{M}_p = 3.0$; dashed), and M3 ($\mathcal{M}_p = 5.0$; solid) are compared to show the dependence on the orbital speed for a fixed wind model. For reference, the dotted line exhibits the sinusoidal function for the perfectly uniform density distribution.

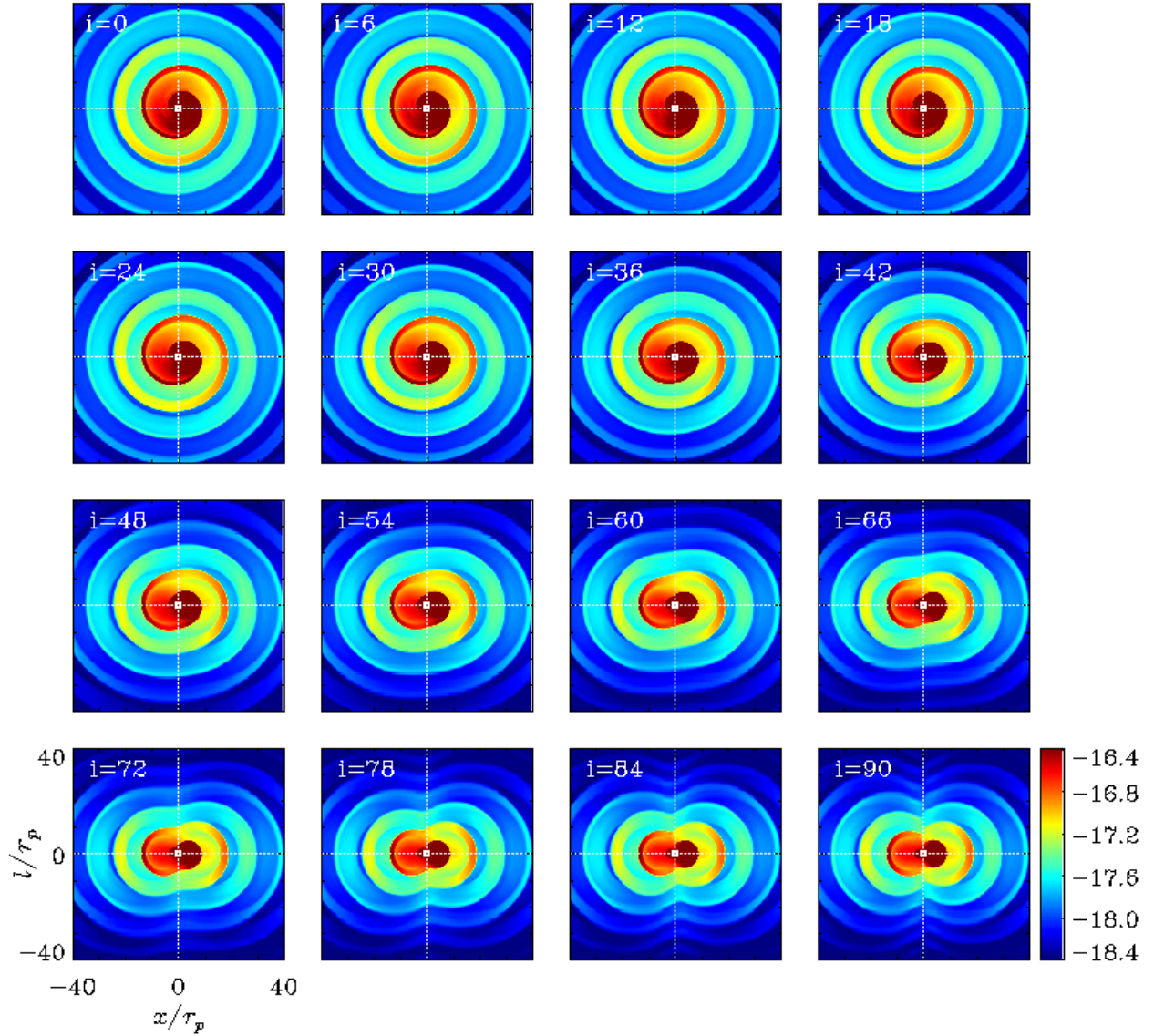


Fig. 7.— Density distribution maps for model M3 as a function of the viewing inclination angle i . The vertical axis is defined by $l = y \cos i + z \sin i$, where z represents the orbital axis. All lengths are scaled to the orbital radius r_p of the mass losing star about the center of mass. Color bar labels the density in unit of $g\text{ cm}^{-3}$ in logarithmic scale.

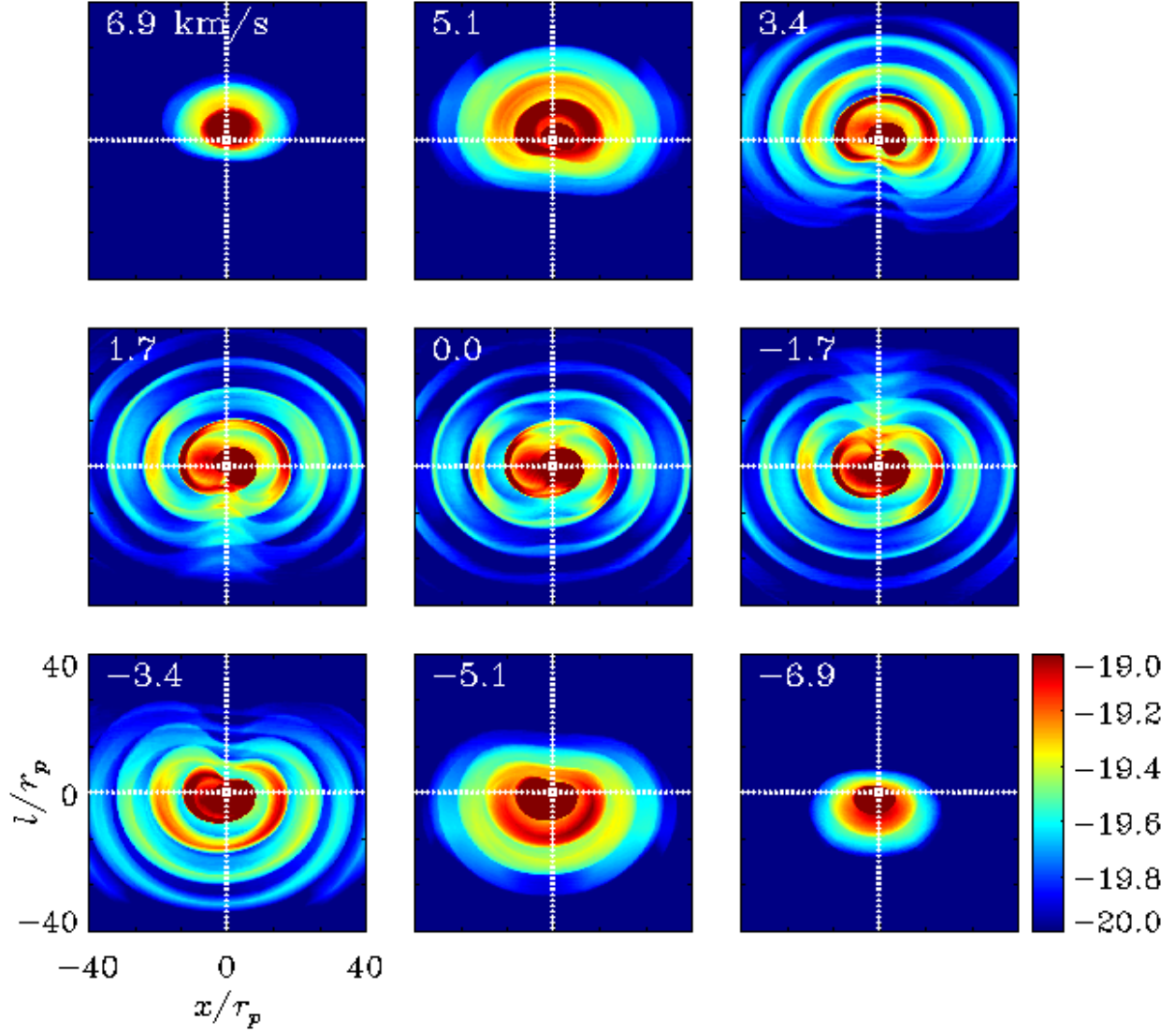


Fig. 8.— Velocity channel map for model M3 with a viewing inclination of 60° . The color bar refers to the integrated density normalized by the total range of velocity (15.4 km s^{-1}) and the domain size (800 AU) in unit of $g\text{ cm}^{-3}$ in logarithmic scale. The central velocity of each channel is denoted on the top left of each panel. The channel width is 1.7 km s^{-1} .

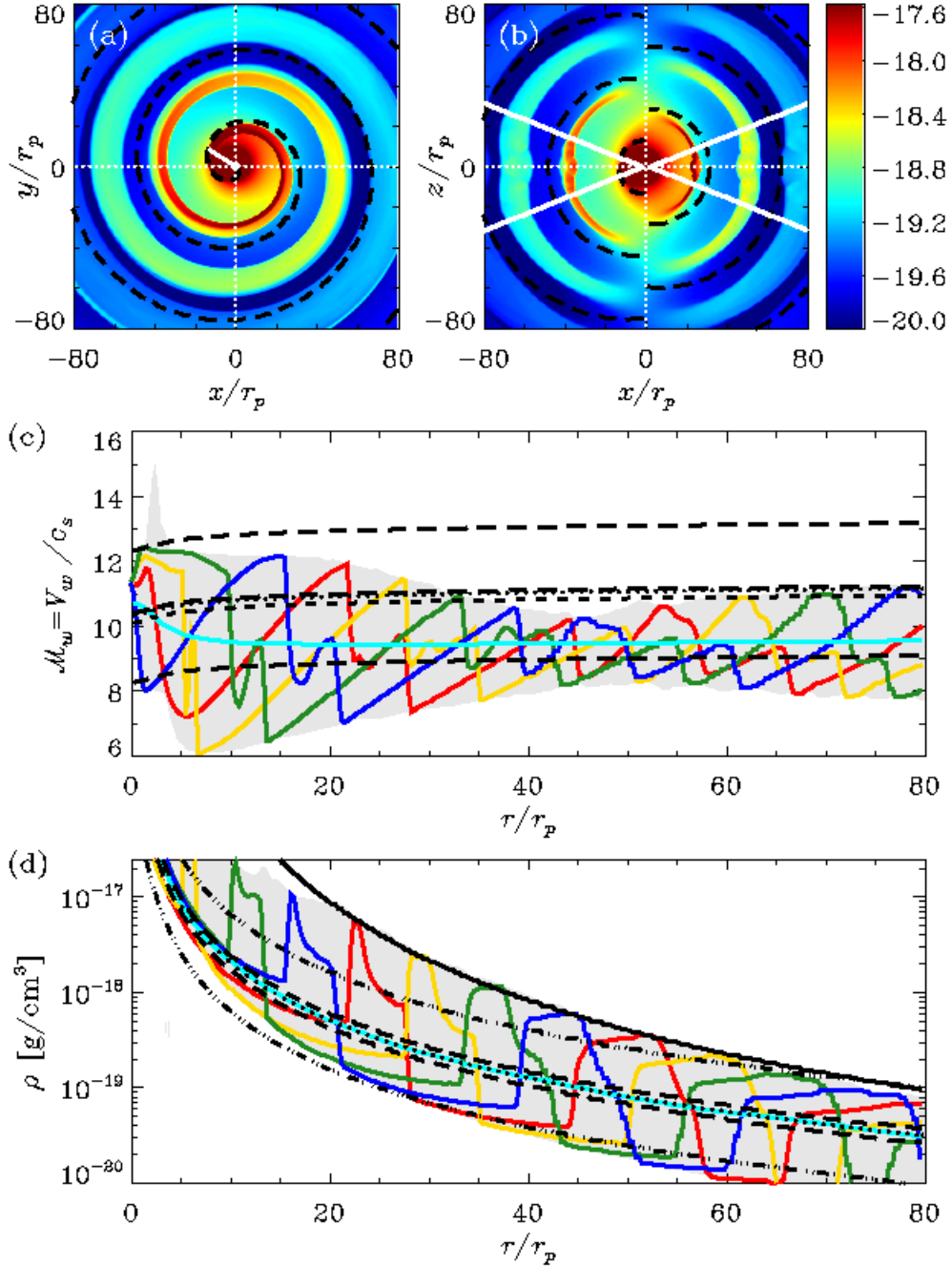


Fig. 9.— Same as Figure 4, but for model M7 including the direct effect of the companion forming a gravitational wake. The dashed lines in (a) and (b) refer to the lines in Figure 4(a)–(b), for comparison with the shapes in model M6 excluding the companion’s direct effect. Note that the shape of the outer shock can be well formulated by, in the pattern propagation speed (Eq. (5)), replacing $V_{w,0}$ (dotted line in (c)) by V_w as the average profile of actual wind velocity. The white line in (b) is the vertical extension limit of the companion wake (See KT12). The black solid line in (d) shows the linear superposition of the maximum density fluctuations caused by the orbital motions of the individual stars.

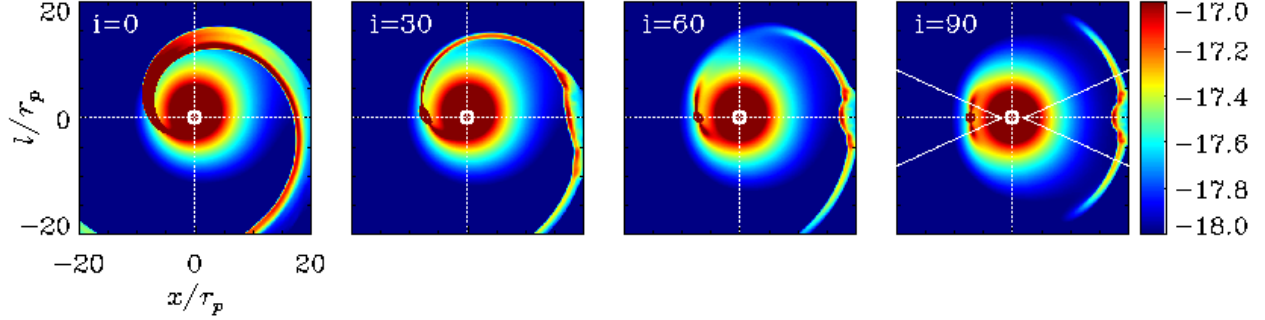


Fig. 10.— Density distribution in the midplane of the sky for model M7 with the viewing inclination angles of 0° , 30° , 60° , and 90° . The gravitational density wake of companion overlapped with the structure due to the reflex motion of the mass losing star creates the sub-arm structures creating a dense inner arm in the face-on view, but appearing as clumpy structures in the inclined views. The white lines on the rightmost panel display the vertical extension limit of the companion wake from (KT12). The white thick circles represent the orbital radius r_p of the mass losing star, and the companion is orbiting at $2r_p$. The vertical axis shows the projected distance, $l = y \cos i + z \sin i$, where z represents the orbital axis. The density in unit of $g \text{ cm}^{-3}$ is color-coded in logarithmic scale.

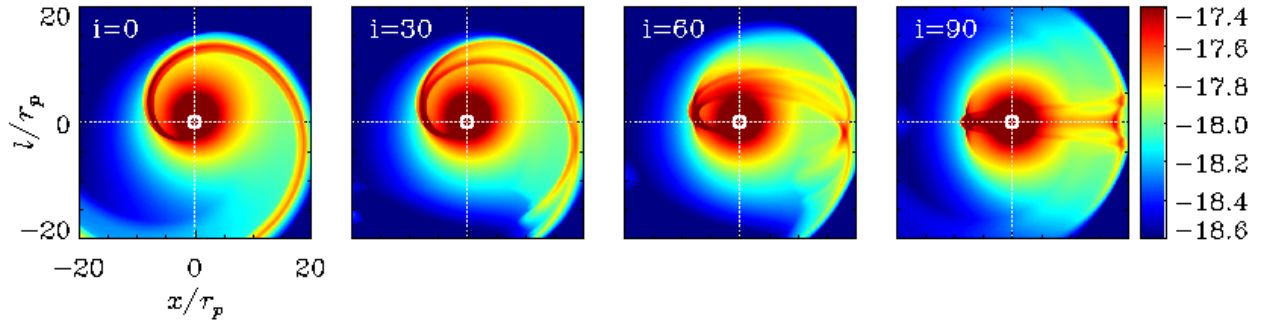


Fig. 11.— Same as Figure 10, but for the average density calculated by the column density over the domain size.